Title

3D in vivo dose verification in prostate proton therapy with deep learning-based proton-acoustic imaging

Journal

Physics in Medicine and Biology, 67(21)

ISSN

0031-9155

Authors

Jiang, Zhuoran
Sun, Leshan
Yao, Weiguang
et al.

Publication Date

2022-11-07

DOI

10.1088/1361-6560/ac9881

Peer reviewed

HHS Public Access

Author manuscript

Phys Med Biol. Author manuscript; available in PMC 2023 October 27.

Published in final edited form as:

Phys Med Biol. ; 67(21): . doi:10.1088/1361-6560/ac9881.

3D In Vivo Dose Verification in Prostate Proton Therapy with Deep Learning-based Proton-acoustic Imaging

Zhuoran Jiang[1,2,+], **Leshan Sun**[3,+], **Weiguang Yao**[4], **Q. Jackie Wu**[1,2], **Liangzhong Xiang**[3,5,6,*], **Lei Ren**[4,*]

[1]Medical Physics Graduate Program, Duke University, Durham, NC, 27705, USA

[2]Department of Radiation Oncology, Duke University Medical Center, Durham, NC, 27710, USA

[3]Department of Biomedical Engineering, University of California, Irvine, California 92617, USA

[4]Department of Radiation Oncology, University of Maryland, Baltimore, MD, 21201, USA

[5]Department of Radiological Sciences, University of California, Irvine, CA 92697, USA

[6]Beckman Laser Institute & Medical Clinic, University of California, Irvine, Irvine, CA 92612, USA

Abstract

Dose delivery uncertainty is a major concern in proton therapy, adversely affecting the treatment precision and outcome. Recently, a promising technique, proton-acoustic (PA) imaging, has been developed to provide real-time *in-vivo* 3D dose verification. However, its dosimetry accuracy is limited due to the limited-angle view of the ultrasound transducer. In this study, we developed a deep learning-based method to address the limited-view issue in the PA reconstruction. A deep cascaded convolutional neural network (DC-CNN) was proposed to reconstruct 3D high-quality radiation-induced pressures using PA signals detected by a matrix array, and then derive precise 3D dosimetry from pressures for dose verification in proton therapy. To validate its performance, we collected 81 prostate cancer patients' proton therapy treatment plans. Dose was calculated using the commercial software RayStation and was normalized to the maximum dose. The proton-acoustic simulation was performed using the open-source k-wave package. A matrix ultrasound array with 64×64 sensors and 500kHz central frequency was simulated near the perineum to acquire radiofrequency (RF) signals during dose delivery. For realistic acoustic simulations, tissue heterogeneity and attenuation were considered, and Gaussian white noise was added to the acquired RF signals. The proposed DC-CNN was trained on 204 samples from 69 patients and tested on 26 samples from 12 other patients. Predicted 3D pressures and dose maps were compared against the ground truth qualitatively and quantitatively using root-mean-squared-error (RMSE), gamma-index (GI), and Dice coefficient of isodose lines. Results demonstrated that the proposed method considerably improved the limited-view proton-acoustic

[*]Authors to whom any correspondence should be addressed, lren@som.umaryland.edu (Lei Ren) and liangzhx@hs.uci.edu (Liangzhong Xiang).

[+]Contributed equally

Ethical statements

All patient data included in this study are anonymized and collected under an IRB protocol approved by University of Maryland. Consent was given for publication by all participants. No clinical trial is involved in this work. The research was conducted in accordance with the principles embodied in the Declaration of Helsinki and in accordance with local statutory requirements.

image quality, reconstructing pressures with clear and accurate structures and deriving doses with a high agreement with the ground truth. Quantitatively, the pressure accuracy achieved an RMSE of 0.061, and the dose accuracy achieved an RMSE of 0.044, GI (3%/3mm) of 93.71%, and 90%-isodose line Dice of 0.922. The proposed method demonstrates the feasibility of achieving high-quality quantitative 3D dosimetry in proton-acoustic imaging using a matrix array, which potentially enables the online 3D dose verification for prostate proton therapy.

Keywords

3D dosimetry; prostate proton therapy; proton-acoustic imaging; matrix ultrasound array; deep learning

1. Introduction

Protons deposit more energy as they slow down, leading to a peak (known as the “Bragg Peak”) near the end of the range of the proton beam. Beyond the peak, dose falls off quickly. This characteristic allows proton therapy to potentially achieve significant healthy tissue sparing beyond the Bragg Peak with the dose concentrated to the target. However, proton therapy is highly susceptible to the delivery errors caused by patient positioning variations and anatomy motions/changes, as well as the systematic errors caused by range uncertainties in dose calculation. The sharp dose fall-off makes proton therapy much more sensitive to these errors than photon therapy, as a small delivery error can cause a significant underdose to the tumor or overdose to healthy tissues. Daily imaging and adaptive therapy can help alleviate the treatment uncertainties, but they all have their own limitations. Daily image, such as cone-beam CT (CBCT), is mostly acquired before the treatment; therefore, it cannot account for intrafraction motions or positioning changes. So far, there is no real-time 3D imaging that can verify intrafraction treatment delivery accuracy. Adaptive therapy is done solely offline in practice due to various challenges for online adaptive proton therapy. Besides, offline adaptive therapy is only done when the anatomy has large deviations since it is a time-consuming and labor-intensive task; therefore, it does not fully address the impact of daily variations. In addition, neither daily CBCT nor adaptive therapy addresses the issue with proton dose calculation uncertainties. Due to all these remaining uncertainties, larger-than-desirable treatment margins are commonly added around the tumor in practice to ensure adequate dose coverage. These margins significantly increase the dose to adjacent healthy tissues (some may even receive the full treatment dose), leading to an increase in radiation-induced toxicities. Concerns of increased toxicities, in turn, constrain the dose that can be prescribed to the tumor and thus limit the tumor control we can achieve. For example, proton radiation therapy (RT) for prostate cancer using standard margins (~1 cm) for treatment uncertainty mitigation resulted in ≥ grade 2 rectal toxicity rates of 15%–22% [1,2]. However, studies have shown that if margins could be reduced to ~2 mm, then rectal toxicity rates could be reduced by up to 50% [3]. Therefore, it is important to verify the dose delivery of proton therapy so that treatment errors can be detected and corrected to minimize their impact, and treatment margins can be reduced to fully explore the true potential of proton therapy.

To address this clinical need, various *in-vivo* dose verification techniques have been proposed to estimate the deposited dose. These techniques can be divided into direct and indirect methods based on the measured signals. (1) Direct methods verify the proton range by directly measuring the dose or fluence. For example, implantable dosimeters/markers with wireless reading [4–6] have been investigated for range verification in proton therapy. These methods only provide limited point dose measurement without 3D volumetric information for dose verification, which is crucial for verifying the tumor and organ at risk (OAR) dose in proton therapy. Besides, these methods require the implantation of dosimeters, which is invasive. (2) Indirect methods verify proton range by measuring the surrogate signals induced by the proton irradiation. Positron emission tomography (PET) [7–10] and prompt gamma (PG) imaging [11–15] have been developed to detect the gammas emitted from the positron emitters or excited nuclei generated along the proton beam path during treatment for range verification. Although annihilation gamma signal is initially correlated to dose deposition, the correlation of the resulting PET images to the delivered dose is severely degraded by biological washout and low signal intensity [16]. PG imaging is still under investigation with challenges of the degradation of PG data caused by false events and misordering, and lack of true 3D information in the PG images [17,18]. Magnetic resonance imaging (MRI) [19,20] is also utilized to detect the tissue constitution changes caused by radiation. However, the MRI device is expensive and not available in the proton therapy room, and therefore it cannot provide in vivo range verification during the treatment delivery.

Recently, acoustic imaging has been investigated to detect proton-induced radiofrequency (RF) signals. When tissues absorb heat from pulsed proton beams, they expand and result in the generation and propagation of acoustic waves, which can be detected by ultrasound transducers and used to reconstruct the radiation-induced pressures. This technique has drawn attention due to its low cost of devices, easy deployment, and capability of real-time dose verification. Ahmad et al. [21] used an analytical model to calculate the proton dose distribution and local pressure rise for beams of different energy (100 and 160 MeV) and spot widths (1, 5, and 10 mm) in a water phantom. Jones et al. [22] first observed acoustic emissions from proton beams using a clinical cyclotron, demonstrating possibilities of the *in-vivo* proton range verification in clinical settings. Assmann et al. [23] performed a simulation study to detect the Bragg Peak position by measuring the RF signals of single proton pulses and achieved sub-millimeter accuracy in localizing the Bragg Peak in a water phantom. However, this study only explored 1D range verification using a single ultrasound transducer without 3D dose volumetric information. Besides, using a water phantom, this study did not account for the heterogeneity of human tissues. Freijo et al. [24] developed a dictionary-based method to achieve proton range verification based on proton-acoustic signals. They performed a simulation study in the 2D computed tomography (CT) images, lacking 3D dose verification. Peng's group conducted several simulation studies [25–27] to verify proton range in 2D or 3D CT images using sparse-view ultrasound detectors distributed over a full 360-degree ring, demonstrating sub-millimeter Bragg peak errors. However, sparse-view detectors in a ring geometry are impractical to deploy during the dose delivery in proton therapy due to the mechanical clearance issue and interference with the treatment delivery. Recently, matrix array has been developed for ultrasound imaging

[28]. It enables real-time 3D imaging while being easy to deploy in clinical settings without mechanical issues or interference with the treatment. A study from our group [29] showed the feasibility of using a transperineal matrix ultrasound array for prostate dose verification. However, the reconstructed pressure maps are distorted due to the limited-angle view of the matrix array, adversely affecting the dose verification accuracy.

Reconstructing images from limited-angle acquisitions is essentially an ill-conditioned inverse problem, in which deep learning has demonstrated great merits [30–35]. Huang et al. [36] developed a deep learning model to reconstruct CT images from limited-angle acquisitions, achieving significantly improved root mean squared errors (RMSE). Our previous study [37] demonstrated the effectiveness of deep learning in restoring volumetric information from limited-angle CBCT. Cheng et al. [38] showed the feasibility of deep learning to reconstruct the 2D speed of sound images for limited-angle ultrasound tomography using phantom data. The results are promising, although the image quality is still degraded.

Considering the advantages of deep learning in the limited-angle reconstruction, in this study, we developed a deep cascaded convolutional neural network (CNN) to generate high-quality 3D pressure maps from limited-angle view ultrasound acquisition, and then predict accurate 3D dose maps from pressure maps for proton therapy dose verification. The cascaded CNN was jointly trained to achieve an optimal end-to-end performance [39–41]. Its performance was tested on the proton-acoustic acquisition simulated using the CT images and clinical treatment plans of prostate cancer patients who underwent proton therapy. To our knowledge, this is the first time that accurate 3D pressure maps are reconstructed from the RF signals acquired by a matrix ultrasound array, and the first time that precise quantitative 3D dosimetry is achieved in the proton-acoustic imaging. The proposed method potentially enables real-time 3D dose verification during proton therapy to significantly improve its precision and outcomes.

2. Methods

2.1 Problem Formulation

2.1.1 Principles—Principles of proton-acoustic signal generation and propagation have been widely investigated and discussed in previous works [42,43]. In brief, proton deposits energy when traveling through tissues, which causes tissue temperature to rise and generates acoustic signals. Under the assumptions of thermal confinement, the process can be modeled as

$$\left(\nabla^2 - \frac{1}{c^2}\frac{\partial^2}{\partial t^2}\right) p(\vec{r}, t) = -\frac{\beta\rho}{C_p}\frac{\partial D(\vec{r}, t)}{\partial t} \quad (1)$$

where $p(\vec{r}, t)$ denotes the acoustic pressure at location $\vec{r}$ and time t, c is the speed of sound, β is the thermal expansion coefficient, ρ is the density of the medium, C_p denotes the medium's heat capacity at a constant pressure, and $D(\vec{r}, t)$ is the dose deposition per unit time.

The amplitude of the proton-induced acoustic signal is proportional to the proton dose deposition per unit time in tissue when both thermal confinement and stress confinement are satisfied [44]. Therefore, for each proton pulse, the relationship between the initial pressure $p_{0\delta}(\vec{r})$ and the dose deposition rate $D_\delta(\vec{r})$ can be expressed as

$$p_{0\delta}(\vec{r}) = \Gamma D_\delta(\vec{r})\rho \tag{2}$$

where $\Gamma = c^2\beta/C_p$ is the Grüneisen parameter, which describes the thermodynamic property of material, $D_\delta(\vec{r})$ is the dose deposition for each proton pencil beam, and ρ is the density of the material.

In this study, we aim to verify the fractional dose, $D(\vec{r})$, which is the sum of all the individual proton pencil beam dose deposition.

$$D(\vec{r}) = \sum D_\delta(\vec{r}) \tag{3}$$

Then the corresponding initial pressure $p_0(\vec{r})$ can be expressed as:

$$p_0(\vec{r}) = \Gamma D(\vec{r})\rho \tag{4}$$

With the initial pressure map $p_0(\vec{r})$, based on Eq (1), the acoustic wave propagation can be solved as

$$p(\vec{r}, t) = \frac{\Gamma\rho\partial}{4\pi c\,\partial t}\left(\frac{1}{ct}\int_{S(\vec{r},t)} D\left(\vec{r}', t\right)dS'(t)\right) \tag{5}$$

where $S'(t)$ denotes a spherical surface that all points on the surface satisfy $|\vec{r} - \vec{r}'| = ct$.

2.1.2 Formulation—Let $x_1 \in R^{I\times J\times K}$ be the real-valued limited-angle reconstructed pressure map with dimension $I\times J\times K$ voxels, and $y_1 \in R^{I\times J\times K}$ be the corresponding ground truth pressure map, and $y_2 \in \mathrm{R}^{I\times J\times K}$ be the corresponding ground truth dose map. According to the above principles, the aimed task can be formulated as finding a pressure restoring pattern f_1 between the limited-angle reconstructed pressure map x_1 and the ground truth pressure map y_1, and a dose correction pattern f_2 between the intermediate dose map $x_2 = \left(\frac{f_1(x_1)}{\rho\times\Gamma}\right)$ (according to Eq(4)) and the ground truth dose map y_2 so that

$$\underset{f_1, f_2}{\operatorname{argmin}}(\lambda_1 \overbrace{\|f_1(x_1) - y_1\|_2^2}^{\substack{pressure\\ restoration}} + \lambda_2 \overbrace{\|f_2(x_2) - y_2\|_2^2}^{dose\ correction}) \tag{6}$$

where ρ denotes the tissue density, Γ denotes the Grüneisen parameters defined in Eq (2), λ_1 and λ_2 are the weighting factors for the pressure loss and the dose loss, respectively.

2.2 Overall Workflow of the Proposed Proton-acoustic Reconstruction and Dose Verification

Based on the above problem formulation, a deep cascaded CNN is proposed in this study to reconstruct pressure and dose maps using a matrix ultrasound array. The overall workflow is shown in Fig. 1. Sequentially, 3D pressure maps are reconstructed using the iterative time-reversal (TR) algorithm [45] from the limited-view RF signals, and are fed into the first model to correct distortions and restore volumetric pressure information. And then the predicted pressure maps are divided by the dose coefficient to generate intermediate dose maps, whose residual errors are further corrected by the second model to achieve the final predicted 3D dose maps.

The two models are cascaded and work jointly for optimized end-to-end performance. For each model, the multi-scale U-Net architecture is used. Based on the original U-Net [46], we made several major changes. (1) In order to restore volumetric information from the TR-based pressures, we adopted 3D convolutional layers instead of 2D convolutional layers. (2) Intensity distribution varies from sample to sample due to the anatomy and dose value changes. To standardize the inputs to each layer, we added batch normalization layers after convolutional layers. This technique has been widely discussed to be helpful in stabilizing and accelerating the training process with higher learning rates. (3) Limited-view reconstruction is severely ill-conditioned. To avoid overfitting, we used dropout layers in the bottom of the U shape. By randomly enabling the feature connections, dropout layers result in varied network architecture during the training process, which potentially helps improve the network robustness and reduce overfitting. More details about the U-shape network in this study are shown in Fig. 2.

3. Experiment Design

To validate the effectiveness of the proposed method in pressure reconstruction and dose verification, the model's performance was evaluated using the proton prostate patient data.

3.1 Proton-acoustic Simulation

The proton-acoustic simulation workflow in this study is shown in Fig. 3. For each patient, CT images and the corresponding treatment plans were anonymized and collected. Dose map on each scan was calculated using a commercial software, the RayStation (RaySearch Laboratories, Stockholm/Sweden), and normalized to the maximum dose. The pressure map was calculated by multiplying the deposited dose, tissue density, and the Grüneisen parameter derived from the CT images. Generation and propagation of the proton-acoustic signals were simulated using the open-source k-wave toolbox [47]. A 2D matrix ultrasound array was simulated to receive acoustic signals during dose delivery. It was placed right below the prostate and near the perineum, with a 30° tilt relative to the patient superior-inferior direction to get a better acoustic window by avoiding the pelvic bones, as illustrated in Fig. 4. Pressure distribution within a volume of size 12 cm × 12 cm × 14 cm above the matrix array was reconstructed using the iterative TR algorithm (10 iterations), and was fed into the proposed model for quality enhancement and dose map generation. More details of the proton-acoustic simulation are discussed as follows.

3.1.1 Patient Enrollment and Dose Calculation—Data of 81 patients who have prostate cancers and underwent proton therapy in our institution were anonymized and collected for this study under an IRB protocol. For each patient, the planning CT scan, the clinical treatment plan, and up to 8 CT-quality assurance (CT-QA) scans were collected. The enrolled treatment plans have two opposite lateral beams delivering all prescribed doses to the prostate. An example is shown in Fig. 4(a). QA scans were rigidly registered to the planning CT scan. Dose maps were calculated using a commercial software, the RayStation (RaySearch Laboratories, Stockholm/Sweden), and were normalized to the maximum dose.

3.1.2 Volume Segmentation—In this study, the CT volume was segmented into four kinds of materials, including air, fat, soft tissue, and bone, based on HU value thresholding. Air in the pelvis region was overwritten to water to avoid acoustic impedance mismatch [48]. The tissue-specific parameters used in this simulation are shown in the Table 1 [49,50].

3.1.3 Acoustic Simulation—All the acoustic simulation was performed using the open-source k-wave toolbox [47] on Matlab (R2019b). The initial pressure maps (P0) were calculated based on the dose maps, the patient CT segmentation, and the tissue acoustic properties (shown in Table 1) according to Eq (4).

A planar ultrasound transducer array with 64 × 64 transducer elements was placed near the perineum area as shown in Fig. 4(b). The total size of the planar array is 8cm × 8 cm, which is large enough to cover the whole prostate area. To simulate realistic acquisitions, the central frequency of the transducer element was set to 500kHz with 100% bandwidth and a sampling rate of 5MHz. Tissue heterogeneity and attenuation (shown in Table 1) were considered during the simulation of the acoustic signal propagation. A Gaussian white noise (10dB signal-to-noise ratio (SNR)) was added to the acquired RF signals.

To balance between the image resolution and memory consumption, all the volume data were resampled to 1.25 mm × 1.25 mm × 1.25mm. Thus, the grid size was set to 96 × 96 × 112. In addition, a 6-pixel perfectly matched layer (PML) was adopted in the simulation.

3.1.4 TR-based Pressure Reconstruction—The pressure maps, which were used as the input of the proposed DC-CNN, were reconstructed from the RF signals acquired by the matrix array using the TR algorithm [45] in the k-wave toolbox. Compared to the conventional universal back-projection (UBP) algorithm [51], TR further considers the tissue heterogeneity, reconstructing more accurate results. In this study, CT-segmented structure maps were used in the TR reconstruction to account for the heterogeneous tissue acoustic properties.

To further improve the model input quality, an iterative TR algorithm was used for the pressure reconstruction. In each iteration, RF signal detection was calculated based on the reconstructed pressure map, and was compared to the real acquired RF signals. The RF signal differences were back-projected to reconstruct a residual pressure which was added to the current pressure to update the pressure map. The iteration was ended by either reaching the maximum iteration number of 10 or meeting the stopping criteria that the RF signal difference was less than 10%.

3.2 Model Training

The proposed model was trained on a dataset containing 204 samples from 69 patients. 10% of the samples in the training dataset were used as validation data to monitor the training process and determine the best checkpoint.

In the training process, the TR-reconstructed limited-angle pressure maps and dose coefficient maps were used as inputs to the proposed model, as demonstrated in Fig. 1. Model weights were optimized by minimizing the mean squared error (MSE) between the predicted and ground truth pressure maps and MSE between the predicted and ground truth dose maps. The loss weights in Eq (6) were empirically set to 2×10^{-6} and 1 for the pressure loss and the dose loss, respectively, according to the dynamic range of their values. The optimizer was set to "Adam" [52]. The learning rate was set to 0.001 and was gradually reduced to 0.0001. The batch size was set to 1 due to the memory limitation.

3.3 Model Evaluation

3.3.1 Evaluation of the Enhancement Performance—The proposed model was tested on 26 samples from another 12 patients. Dose calculation and acoustic simulation followed the process mentioned in section 3.1. For each testing case, initial pressure map was reconstructed from the RF signals using the iterative TR algorithm and was then fed into the trained model to predict enhanced pressure maps and dose maps, which were compared to the corresponding ground truth for evaluation.

3.3.2 Evaluation of the Robustness against SNR—The SNR of RF signals can vary due to the background noise variations. In previous proton-acoustic studies [21,26,53,54], most SNRs were set to 5~30dB. Thus, in this study, SNR was set to 5dB, 10dB, 15dB, 20dB, and 30dB for each testing case to further validate the method's robustness against the signal noise levels. The other simulation configurations except the SNR were kept the same as described in section 3.1. The predicted pressure and dose maps were compared among different SNRs as well as to the ground truth. Note that the proposed deep learning framework was trained on the data with an SNR of 10dB. Once the framework was trained, no further re-training or finetuning was performed to adapt to the new noise levels in the testing process.

3.4 Evaluation Metrics

The predicted pressure and dose maps were compared to the corresponding ground truth maps both qualitatively and quantitatively using root mean squared errors (RMSE). To further validate the performance of the proposed method in dose verification, we evaluated the predicted dose maps using the isodose line Dice coefficient and the gamma index.

The Dice coefficient, which is also referred to as the overlap index, is a widely used metric in validating segmentation accuracy. In this study, we extracted the isodose lines (including 10%, 25%, 50%, 75%, and 90%) from dose maps and calculated the Dice coefficients of the areas within isodose lines between the predicted and ground truth dose maps.

The gamma index is used to evaluate the coincidence between the predicted and the ground truth dose maps by calculating both the dose difference and the distance difference. In this study, the global gamma index analysis was performed with 3%/3mm, 2%/3mm, 3%/5mm and 2%/5mm thresholds.

4. Results

4.1 Pressure Enhancement and Dose Prediction

Fig. 5 shows a representative case in different slices and the 3D views. Due to the limited view of the ultrasound matrix array, pressures reconstructed by the iterative TR algorithm showed severe distortions, in which structures can hardly be distinguished from the artifacts. Our proposed method effectively removed artifacts and corrected distortions, considerably improving the pressure map quality with accurate and clear structures and edges. Compared to the ground truth pressure maps, our method restored most of the volumetric information precisely. And the predicted dose maps based on the predicted pressures agreed very well with the ground truth dose maps.

Table 2 shows the quantitative results of the predicted pressure and dose maps of our proposed method. Metric values are calculated from all the 26 cases from 12 testing patients. Both the predicted pressure maps and the dose maps showed low-intensity errors compared to the ground truth. The predicted dose maps showed a high similarity of the isodose lines compared with the ground truth, as indicated by the isodose line Dice coefficients. Results also showed a high agreement between the predicted and the ground truth 3D dose maps, as indicated by the high gamma index. Quantitative results further confirmed the effectiveness of the proposed method.

4.2 Robustness against SNRs

Fig. 6 shows representative slices of a testing case with different SNRs. For both the pressure maps and the dose maps, little changes were observed as SNR increased from 5dB to 30dB. Fig. 7 shows the boxplot of the evaluation metrics of all testing cases. Marginal variations were shown among different SNRs. Both the qualitative and quantitative results demonstrated the robustness of the proposed method against the SNRs.

The robustness results from two main reasons. First, the input pressure maps to the proposed method are reconstructed using the iterative time-reversal algorithm, whose performance is relatively stable as noise level varies. Second, the proposed models were trained to enhance the noisy data to match with the noise-free ground truth data, which enabled the models to address the noises in the input images.

4.3 Runtime

The proposed cascaded deep learning model was implemented using the Keras framework with Tensorflow backend. The model training and testing were performed on a computer equipped with a CPU of Intel Xeon and 32GB memory and a GPU of NVIDIA Titan RTX (24GB memory). The pressure enhancement and dose prediction with the proposed method are fully automatic, which takes about 0.22 second in total.

5. Discussion

Proton-acoustic imaging is a promising technique to achieve real-time dose verification to reduce the delivery uncertainties of proton therapy. Although the matrix array-based ultrasound reconstruction enables real-time 3D imaging of the target, it inevitably introduces distortions to the images due to its limited-angle views. In this study, we proposed a deep learning-based method to restore volumetric pressure and dose information from the limited-view acquisition of a matrix array. Our study demonstrated the effectiveness and efficiency of the proposed deep cascaded CNN model in predicting high-quality pressure maps using the pressure maps reconstructed from RF signals acquired by a matrix array and in deriving precise 3D dose maps from the predicted pressure maps.

The proposed method can provide a valuable tool for the online dose verification of prostate proton therapy during the treatment delivery. The transperineal ultrasound matrix array is convenient to deploy in the current RT workflow and has minimal impact on the treatment beam planning. During the treatment, radiation-induced RF signals can be acquired by the ultrasound array and used to reconstruct pressure maps, from which dose deposition maps are derived for dose verification. In this study, we focused on validating the feasibility of the proposed method in generating the 3D accumulated fractional dose for interfraction treatment verification, which is crucial for daily treatment assessment and adaptive therapy in the clinical RT workflow. In the future, we would like to further investigate the capabilities of the method for verifying the dose delivered by individual proton pencil beams for intrafraction treatment verification, which can be valuable for minimizing dose deviations caused by intrafraction variations.

In this study, since the reconstructed pressure map is used as the input of the pressure map prediction model, the quality of the input reconstructed map directly affects the output accuracy of the model. The iterative TR algorithm was used for the initial pressure map reconstruction since it achieved superior image quality compared to the TR algorithm. Compared to TR, despite little improvements in correcting distortions, iterative TR reconstructs pressures with higher SNR, which gives us a better starting image and thus leads to a more accurate prediction of the deep learning model. Similar image quality improvement has also been observed in our previous study [34]. In future studies, advanced data-preprocess techniques can be employed to further improve the RF signal quality and/or input image quality, which can further improve the performance of our proposed method.

Besides the dose verification, the proposed method is potentially feasible for the 3D ultrasound image reconstruction using a matrix array, which suffers the same limited-view acquisition issue as this study.

There are some limitations of this study. First, no absolute dose values were achieved by the proposed method. Due to the inter-patient dose variations and the severely degraded pressure quality caused by distortions and noises, it is challenging to restore the absolute dose values. As an alternative, we normalized the dose to its maximum values in this study, and achieved accurate relative dose verification. In future studies, we can take advantages of the patient-specific learning [37,55] to incorporate the patient-specific prior knowledge into

the deep learning models to address this challenge. This strategy has shown effectiveness in addressing severe distortions and pixel value errors from the ill-conditioned reconstruction, and thus can help achieve more accurate absolute dose verification in our tasks. Second, dose coefficient and structure maps are designed to be derived from the in-room CT or onboard CBCT. Regarding onboard CBCT, although its image quality is generally inferior to the CT, numerous methods have been developed to enhance CBCT image quality to be comparable to CT [56–58]. In addition, the HU value variations have a limited impact on the dose coefficient accuracy. As described in section 3.1.2, four kinds of tissues are segmented based on HU value thresholding. As long as the tissue HU value falls into the corresponding range, the segmentation results are accurate, and thus the dose coefficients are correctly assigned. Thirdly, in this simulation study, the air in the pelvis region was overwritten to water to avoid acoustic impedance mismatch, similar to previous studies [48]. In clinical practice, the influence of air can be minimized by adjusting ultrasound array position and orientation, drinking water to fill the bladder, and filling rectum balloons. In future studies, the application of deep learning can be further explored in addressing the air-induced acoustic image quality degradation.

6. Conclusion

The proposed deep cascaded CNN demonstrated the effectiveness and efficiency in substantially enhancing the image quality of the radiation-induced pressures acquired from a limited-view matrix array, as well as in deriving 3D precise quantitative dose deposition maps for *in-vivo* proton therapy dose verification. Besides, the proposed method presented a general workflow for enhancing limited-view image reconstruction, which is potentially applicable for matrix array-based 3D ultrasound imaging for applications in radiology and radiation oncology.

Acknowledgments

This work was supported by the National Institutes of Health under Grant No. R01-CA184173, R01-EB028324, R37CA240806. The content is solely the responsibility of the authors and does not necessarily represent the official views of the National Institutes of Health. This work was also supported by the American Cancer Society (133697-RSG-19-110-01-CCE), and the UCI Chao Family Comprehensive Cancer Center (P30CA062203).

References

1. Bryant CM, Henderson RH, Nichols RC, et al. Consensus Statement on Proton Therapy for Prostate Cancer. 2021;8(2):1–16.
2. Colaco RJ, Hoppe BS, Flampouri S, et al. Rectal toxicity after proton therapy for prostate cancer: an analysis of outcomes of prospective studies conducted at the university of Florida Proton Therapy Institute. 2015;91(1):172–181.
3. Polf JC, Chuong M, Zhang B, Mehta MJIjopt. Anteriorly oriented beam arrangements with daily in vivo range verification for proton therapy of prostate cancer: Rectal toxicity rates. 2016;2(4):509–517.
4. Lu HM, Mann G, Cascio E. Investigation of an implantable dosimeter for single - point water equivalent path length verification in proton therapy. Medical physics. 2010;37(11):5858–5866. [PubMed: 21158298]
5. Telsemeyer J, Jäkel O, Martišíková M. Quantitative carbon ion beam radiography and tomography with a flat-panel detector. Physics in Medicine & Biology. 2012;57(23):7957. [PubMed: 23154641]

6. Bentefour EH, Shikui T, Prieels D, Lu H-M. Effect of tissue heterogeneity on an in vivo range verification technique for proton therapy. Physics in Medicine & Biology. 2012;57(17):5473. [PubMed: 22864304]
7. Fiedler F, Priegnitz M, Juelich R, et al. In-beam PET measurements of biological half-lives of 12C irradiation induced β+-activity. Acta Oncologica. 2008;47(6):1077–1086. [PubMed: 18770062]
8. Fiedler F, Shakirin G, Skowron J, et al. On the effectiveness of ion range determination from in-beam PET data. Physics in Medicine & Biology. 2010;55(7):1989. [PubMed: 20224157]
9. Nishio T, Miyatake A, Ogino T, Nakagawa K, Saijo N, Esumi H. The development and clinical use of a beam ON-LINE PET system mounted on a rotating gantry port in proton therapy. International Journal of Radiation Oncology* Biology* Physics. 2010;76(1):277–286.
10. Miyatake A, Nishio T, Ogino T, Saijo N, Esumi H, Uesaka M. Measurement and verification of positron emitter nuclei generated at each treatment site by target nuclear fragment reactions in proton therapy. Medical physics. 2010;37(8):4445–4455. [PubMed: 20879603]
11. Min C-H, Kim CH, Youn M-Y, Kim J-W. Prompt gamma measurements for locating the dose falloff region in the proton therapy. Applied physics letters. 2006;89(18):183517.
12. Min CH, Lee HR, Kim CH, Lee SB. Development of array-type prompt gamma measurement system for in vivo range verification in proton therapy. Medical physics. 2012;39(4):2100–2107. [PubMed: 22482631]
13. Kormoll T, Fiedler F, Schöne S, Wüstemann J, Zuber K, Enghardt W. A Compton imager for in-vivo dosimetry of proton beams—A design study. Nuclear Instruments and Methods in Physics Research Section A: Accelerators, Spectrometers, Detectors and Associated Equipment. 2011;626:114–119.
14. Polf J, Peterson S, Ciangaru G, Gillin M, Beddar S. Prompt gamma-ray emission from biological tissues during proton irradiation: a preliminary study. Physics in Medicine & Biology. 2009;54(3):731. [PubMed: 19131673]
15. Draeger E, Mackin D, Peterson S, et al. 3D prompt gamma imaging for proton beam range verification. Physics in Medicine & Biology. 2018;63(3):035019. [PubMed: 29380750]
16. Parodi K, Paganetti H, Shih HA, et al. Patient study of in vivo verification of beam delivery and range, using positron emission tomography and computed tomography imaging after proton therapy. International Journal of Radiation Oncology* Biology* Physics. 2007;68(3):920–934.
17. Polf JC, Barajas CA, Peterson SW, et al. Applications of machine learning to improve the clinical viability of Compton camera based in vivo range verification in proton radiotherapy. Frontiers in Physics. 2022:284.
18. Xie Y, Bentefour EH, Janssens G, et al. Prompt gamma imaging for in vivo range verification of pencil beam scanning proton therapy. International Journal of Radiation Oncology* Biology* Physics. 2017;99(1):210–218.
19. Gensheimer MF, Yock TI, Liebsch NJ, et al. In vivo proton beam range verification using spine MRI changes. International Journal of Radiation Oncology* Biology* Physics. 2010;78(1):268–275.
20. Yuan Y, Andronesi OC, Bortfeld TR, et al. Feasibility study of in vivo MRI based dosimetric verification of proton end-of-range for liver cancer patients. Radiotherapy and Oncology. 2013;106(3):378–382. [PubMed: 23473960]
21. Ahmad M, Xiang L, Yousefi S, Xing L. Theoretical detection threshold of the proton-acoustic range verification technique. Medical physics. 2015;42(10):5735–5744. [PubMed: 26429247]
22. Jones KC, Vander Stappen F, Bawiec CR, et al. Experimental observation of acoustic emissions generated by a pulsed proton beam from a hospital-based clinical cyclotron. Medical physics. 2015;42(12):7090–7097. [PubMed: 26632062]
23. Assmann W, Kellnberger S, Reinhardt S, et al. Ionoacoustic characterization of the proton Bragg peak with submillimeter accuracy. Medical physics. 2015;42(2):567–574. [PubMed: 25652477]
24. Freijo C, Herraiz JL, Sanchez-Parcerisa D, Udias JM. Dictionary-based protoacoustic dose map imaging for proton range verification. Photoacoustics. 2021;21:100240. [PubMed: 33520652]
25. Yu Y, Li Z, Zhang D, Xing L, Peng H. Simulation studies of time reversal-based protoacoustic reconstruction for range and dose verification in proton therapy. Medical physics. 2019;46(8):3649–3662. [PubMed: 31199511]

26. Yao S, Hu Z, Zhang X, et al. Feasibility study of range verification based on proton-induced acoustic signals and recurrent neural network. Physics in Medicine & Biology. 2020;65(21):215017. [PubMed: 32726760]
27. Yao S, Hu Z, Xie Q, Yang Y, Peng H. Further investigation of 3D dose verification in proton therapy utilizing acoustic signal, wavelet decomposition and machine learning. Biomedical Physics & Engineering Express. 2021;8(1):015008.
28. Yu J, Yoon H, Khalifa YM, Emelianov SY. Design of a volumetric imaging sequence using a Vantage-256 ultrasound research platform multiplexed with a 1024-element fully sampled matrix array. IEEE transactions on ultrasonics, ferroelectrics, and frequency control. 2019;67(2):248–257. [PubMed: 31545718]
29. Wang M, Samant P, Wang S, et al. Toward in vivo dosimetry for prostate radiotherapy with a transperineal ultrasound array: A simulation study. IEEE transactions on radiation and plasma medical sciences. 2020;5(3):373–382. [PubMed: 33969250]
30. Maier A, Syben C, Lasser T, Riess C. A gentle introduction to deep learning in medical image processing. Zeitschrift für Medizinische Physik. 2019;29(2):86–101. [PubMed: 30686613]
31. Litjens G, Kooi T, Bejnordi BE, et al. A survey on deep learning in medical image analysis. Medical image analysis. 2017;42:60–88. [PubMed: 28778026]
32. Zhang H-M, Dong B A review on deep learning in medical image reconstruction. Journal of the Operations Research Society of China. 2020;8(2):311–340.
33. Chen H, Zhang Y, Chen Y, et al. LEARN: Learned experts' assessment-based reconstruction network for sparse-data CT. IEEE transactions on medical imaging. 2018;37(6):1333–1347. [PubMed: 29870363]
34. Jiang Z, Chen Y, Zhang Y, Ge Y, Yin F-F, Ren L. Augmentation of CBCT reconstructed from under-sampled projections using deep learning. IEEE transactions on medical imaging. 2019;38(11):2705–2715. [PubMed: 31021791]
35. Schlemper J, Caballero J, Hajnal JV, Price AN, Rueckert D. A deep cascade of convolutional neural networks for dynamic MR image reconstruction. IEEE transactions on Medical Imaging. 2017;37(2):491–503. [PubMed: 29035212]
36. Huang Y, Preuhs A, Lauritsch G, Manhart M, Huang X, Maier A. Data consistent artifact reduction for limited angle tomography with deep learning prior. Paper presented at: International workshop on machine learning for medical image reconstruction2019.
37. Jiang Z, Yin F-F, Ge Y, Ren L. Enhancing digital tomosynthesis (DTS) for lung radiotherapy guidance using patient-specific deep learning model. Physics in Medicine & Biology. 2021;66(3):035009. [PubMed: 33238249]
38. Cheng A, Kim Y, Anas EM, et al. Deep learning image reconstruction method for limited-angle ultrasound tomography in prostate cancer. Paper presented at: Medical Imaging 2019: Ultrasonic Imaging and Tomography2019.
39. Jiang Z, Yin F-F, Ge Y, Ren L. A multi-scale framework with unsupervised joint training of convolutional neural networks for pulmonary deformable image registration. Physics in Medicine & Biology. 2020;65(1):015011. [PubMed: 31783390]
40. Yang Y, Hu Y, Zhang X, Wang S. Two-stage selective ensemble of CNN via deep tree training for medical image classification. IEEE Transactions on Cybernetics. 2021.
41. Tajbakhsh N, Jeyaseelan L, Li Q, Chiang JN, Wu Z, Ding X. Embracing imperfect datasets: A review of deep learning solutions for medical image segmentation. Medical Image Analysis. 2020;63:101693. [PubMed: 32289663]
42. Lascaud J, Dash P, Wieser H-P, et al. Investigating the accuracy of co-registered ionoacoustic and ultrasound images in pulsed proton beams. Physics in Medicine & Biology. 2021;66(18):185007.
43. Forghani F, Mahl A, Patton TJ, et al. Simulation of x-ray-induced acoustic imaging for absolute dosimetry: Accuracy of image reconstruction methods. Medical Physics. 2020;47(3):1280–1290. [PubMed: 31828781]
44. Hickling S, Xiang L, Jones KC, et al. Ionizing radiation-induced acoustics for radiotherapy and diagnostic radiology applications. Medical physics. 2018;45(7):e707–e721. [PubMed: 29679491]

45. Hristova Y, Kuchment P, Nguyen L. Reconstruction and time reversal in thermoacoustic tomography in acoustically homogeneous and inhomogeneous media. Inverse problems. 2008;24(5):055006.
46. Ronneberger O, Fischer P, Brox T. U-net: Convolutional networks for biomedical image segmentation. Paper presented at: International Conference on Medical image computing and computer-assisted intervention2015.
47. Treeby BE, Cox BT. k-Wave: MATLAB toolbox for the simulation and reconstruction of photoacoustic wave fields. Journal of biomedical optics. 2010;15(2):021314. [PubMed: 20459236]
48. Jones KC, Nie W, Chu JC, et al. Acoustic-based proton range verification in heterogeneous tissue: simulation studies. Physics in Medicine & Biology. 2018;63(2):025018. [PubMed: 29176057]
49. Yao D-K, Zhang C, Maslov KI, Wang LV. Photoacoustic measurement of the Grüneisen parameter of tissue. Journal of biomedical optics. 2014;19(1):017007.
50. Prince JL, Links JM. Medical imaging signals and systems. Pearson Prentice Hall Upper Saddle River; 2006.
51. Xu M, Wang LV. Universal back-projection algorithm for photoacoustic computed tomography. Physical Review E. 2005;71(1):016706.
52. Kingma DP, Ba J. Adam: A method for stochastic optimization. arXiv preprint arXiv:14126980. 2014.
53. Jones KC, Vander Stappen F, Sehgal CM, Avery SJMp. Acoustic time-of-flight for proton range verification in water. 2016;43(9):5213–5224.
54. Riva M, Vallicelli EA, Baschirotto A, De Matteis MJItobc, systems. Acoustic analog front end for proton range detection in hadron therapy. 2018;12(4):954–962.
55. Jiang Z, Zhang Z, Chang Y, Ge Y, Yin F-F, Ren L. Prior image-guided cone-beam computed tomography augmentation from under-sampled projections using a convolutional neural network. Quantitative imaging in medicine and surgery. 2021;11(12):4767. [PubMed: 34888188]
56. Chen L, Liang X, Shen C, Jiang S, Wang J. Synthetic CT generation from CBCT images via deep learning. Medical physics. 2020;47(3):1115–1125. [PubMed: 31853974]
57. Liu Y, Lei Y, Wang T, et al. CBCT-based synthetic CT generation using deep-attention cycleGAN for pancreatic adaptive radiotherapy. Medical physics. 2020;47(6):2472–2483. [PubMed: 32141618]
58. Chen L, Liang X, Shen C, Nguyen D, Jiang S, Wang J. Synthetic CT generation from CBCT images via unsupervised deep learning. Physics in Medicine & Biology. 2021;66(11):115019.

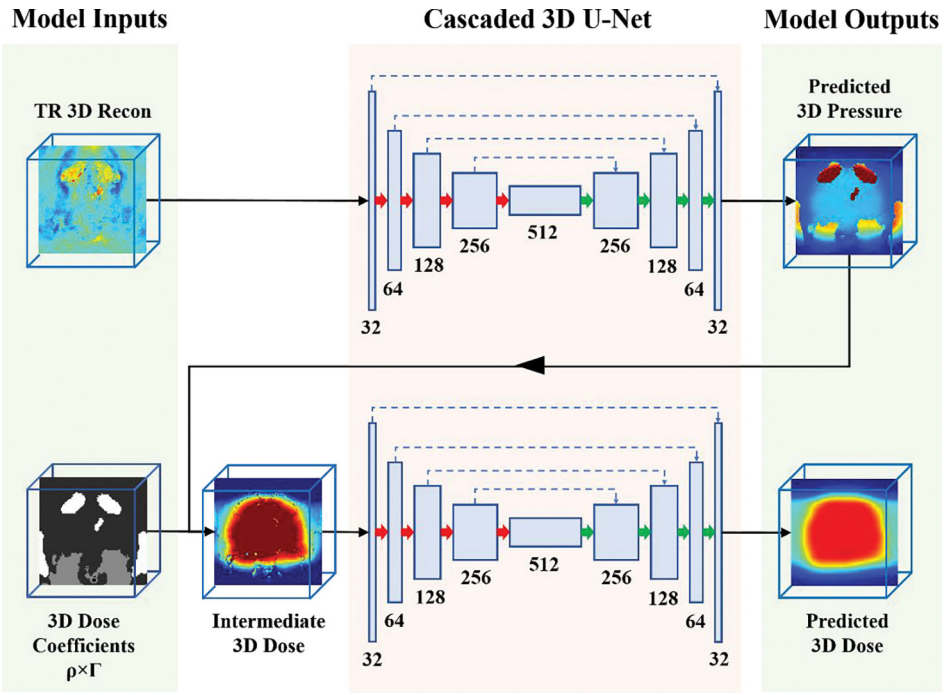

Fig. 1.

Overall workflow of the proton-acoustic pressure and dose map reconstruction using a cascaded 3D U-Net. Numbers under the network layers indicate the data channels.

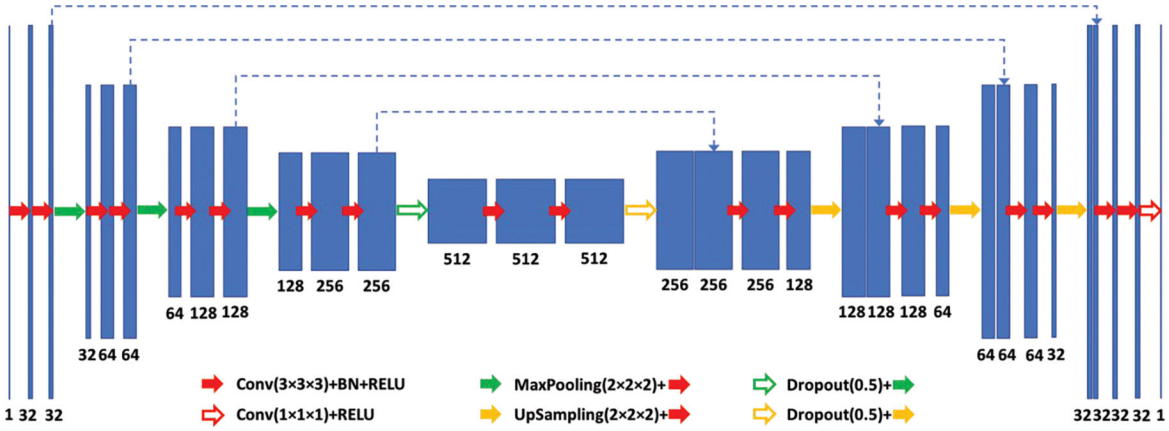

Fig. 2.

The architecture of the U-Net used for the localization model and the enhancement model.

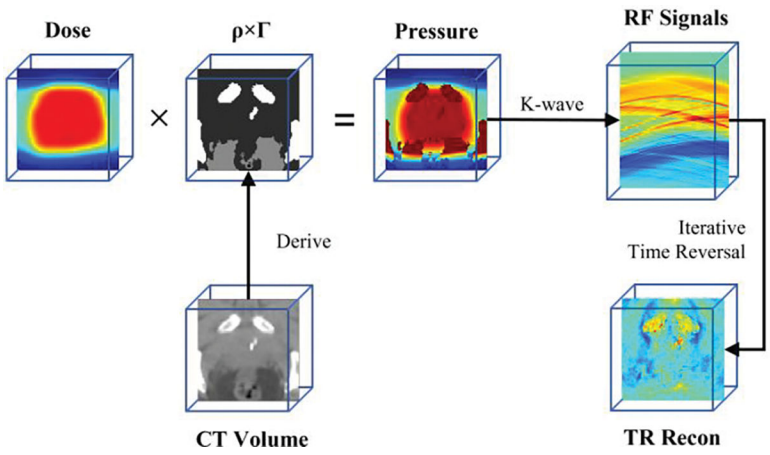

Fig. 3.
Overall workflow of the proton-acoustic simulation.

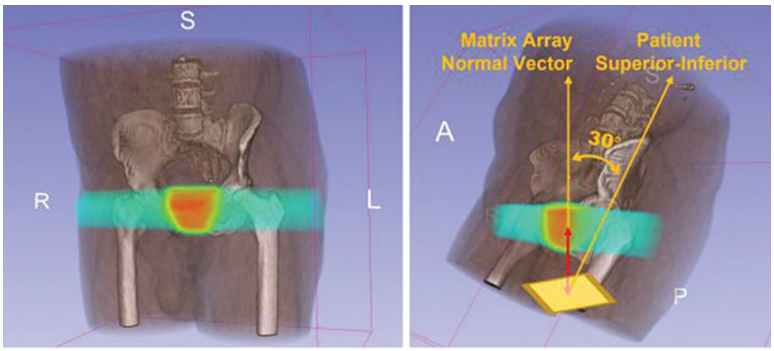

Fig. 4.

Experiment setup. (a) is the volume rendering of the CT images and planning dose of a proton prostate patient. The dose is rendered using the ‘jet’ colormap, where red indicates high dose and blue indicates low dose. (b) shows the matrix ultrasound array placed near the perineum to receive acoustic signals during dose delivery.

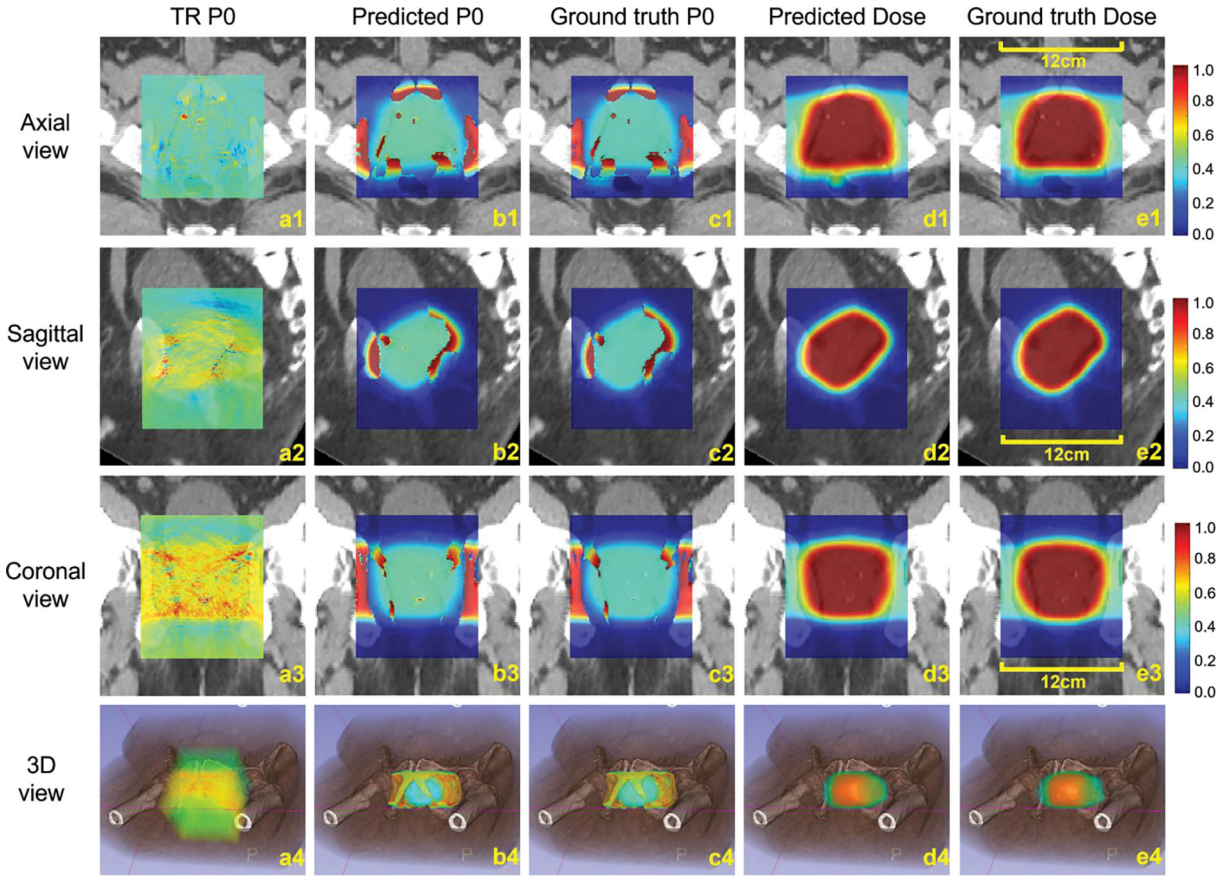

Fig. 5.

Representative slices of the pressure and dose maps. (a) are the pressure maps (P0) reconstructed using the iterative time-reversal (TR) algorithm. (b) are the pressure maps predicted by the proposed method. (c) are the ground truth pressure maps. (d) are the dose maps predicted by the proposed method. (e) are the ground truth dose maps. The 'jet' color map is used for (1–3) which is shown as the right-side color bar. For the 3D view rendering shown in (4), the pressures shown in (a4-c4) are rendered using the same color/opacity map, the doses shown in (d4-e4) are rendered using the same color/opacity map. The 'jet' color map is used for (4) where red indicates high intensities and blue low.

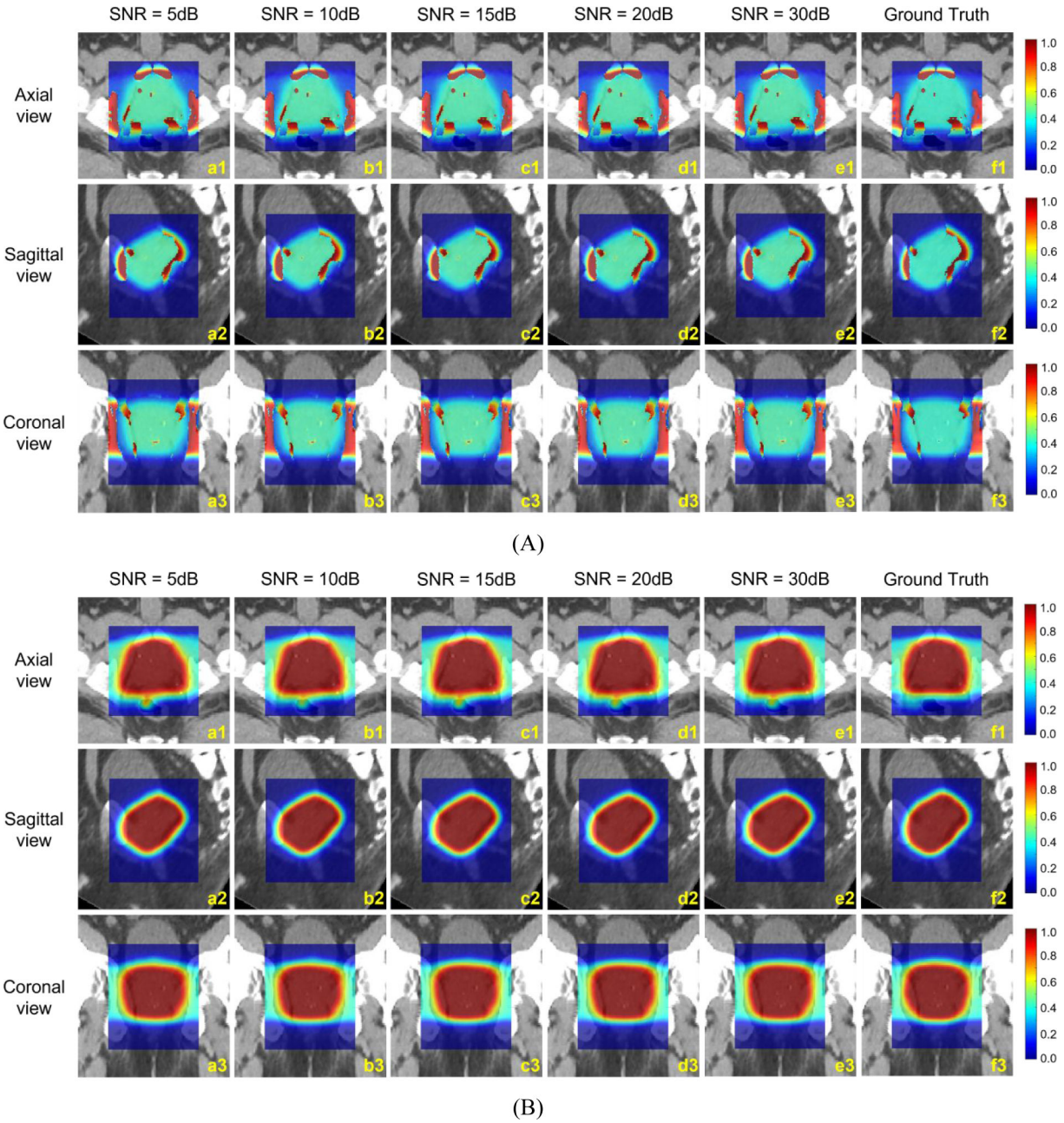

Fig. 6.

Representative slices of (A) the pressure maps and (B) the dose maps predicted by the proposed method from signals of different SNRs. (a) SNR = 5dB, (b) SNR = 10dB, (c) SNR = 15dB, (d) SNR = 20dB, (e) SNR = 30dB, and (f) are the ground truth pressure maps. Color map is shown as the right-side color bar.

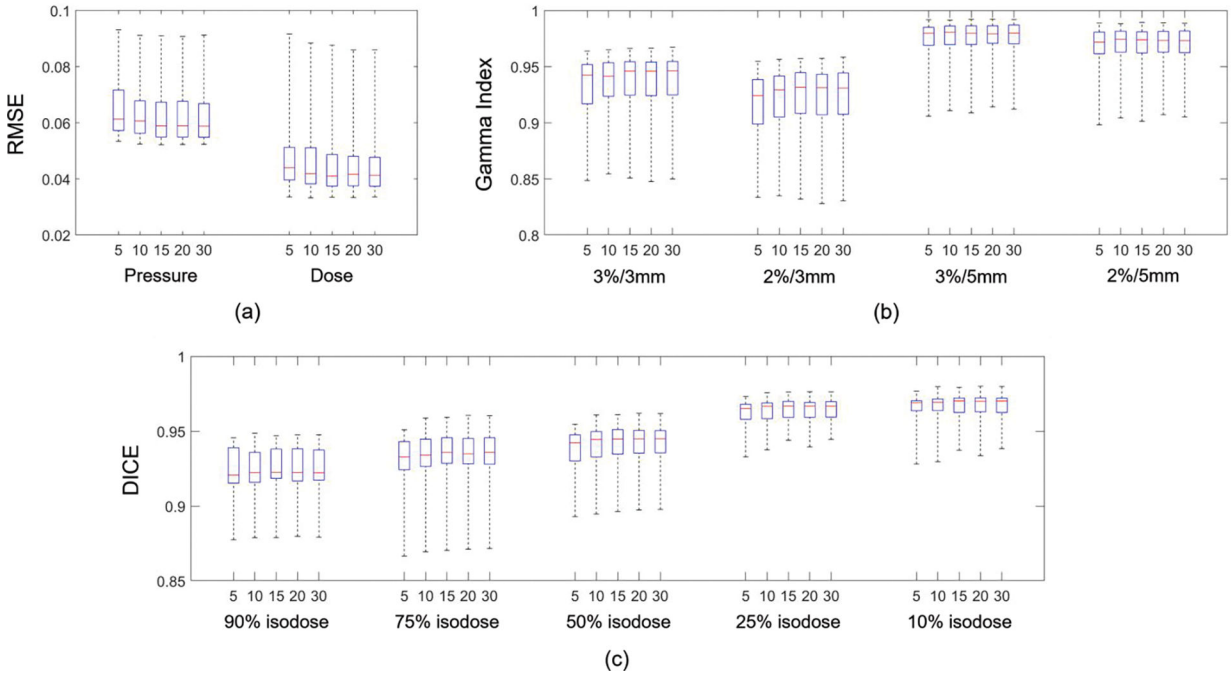

Fig. 7.

Boxplot of the (a) root mean squared error (RMSE) of the predicted pressure maps and predicted dose maps, (b) gamma index of the predicted dose maps, and (c) Dice coefficient of the predicted dose maps using data with SNR of 5dB, 10dB, 15dB, 20dB, and 30dB.

Table. 1.

HU values and thermoacoustic parameters of different tissues.

Tissue	HU value	v (m/s)*	ρ (kg/m^3)+	Γ^	ρ×Γ (kg/m^3)	α (dB/cm/MHz)#
Air	[−1000, −200)	-	-	-	-	-
Water	air overwritten	1500	1000	0.11	110	0.0022
Fat	[−200, −50)	1480	920	0.80	736	0.5
Soft tissue	[−50, 100)	1540	1040	0.30	312	1
Bone	[100, max)	2000	1900	0.80	1520	10

*Speed of sound.

+Tissue density.

^Grüneisen parameter.

#Attenuation coefficient.

Table. 2.

Quantitative analysis of the pressure and dose maps. Metric values are calculated from all 26 testing cases.

Modality	Metric	Value *
Pressure	RMSE	0.062 ± 0.009
Dose	RMSE	0.046 ± 0.013
	90% isodose line Dice	0.923 ± 0.017
	75% isodose line Dice	0.932 ± 0.018
	50% isodose line Dice	0.940 ± 0.014
	25% isodose line Dice	0.963 ± 0.009
	10% isodose line Dice	0.966 ± 0.010
	Gamma index (3%/3mm)	93.30% ± 3.09%
	Gamma index (2%/3mm)	91.89% ± 3.36%
	Gamma index (3%/5mm)	97.34% ± 1.98%
	Gamma index (2%/5mm)	96.72% ± 2.12%

Intensities of pressure and dose maps are normalized to [0, 1] to calculate the metrics.

*Numbers in the table are expressed as mean±standard deviation.